Photocatalytic splitting of water under visible-light irradiation over the NiOx-loaded Sm_2InTaO_7 with $4f$-d^{10}-d^0 configuration

Xinde Tang [a,*], Hongqi Ye [a], Hui Liu [a,b], Chenxia Ma [a], Zhi Zhao [a]

[a] College of Chemistry and Chemical Engineering, Central South University, Changsha 410083, China
[b] State Key Laboratory for Powder Metallurgy, Central South University, Changsha 410083, China

ARTICLE INFO

ABSTRACT

A new visible-light-response photocatalyst Sm_2InTaO_7 with $4f$-d^{10}-d^0 configuration crystallized in a cubic system with the space group $Fd3m$ was synthesized by a solid-state reaction method. NiOx-loaded Sm_2InTaO_7 showed high photocatalytic activities for H_2 evolution from pure water under visible light irradiation ($\lambda > 400$ nm). Changes in the photocatalytic activity with the calcination temperature of Sm_2InTaO_7 and the amount of NiOx loaded indicated that the combination of highly crystallized Sm_2InTaO_7 and a high dispersion of NiOx particles led to high photocatalytic activity. The high photocatalytic performance of NiOx-loaded Sm_2InTaO_7 supported the existing view that the photocatalytic activity correlated with the lattice distortion. Density functional theory calculation indicated that strong dispersion from the hybridized In $5s$ $5p$ orbitals at the bottom of the conduction band was responsible for the high activity of photocatalyst Sm_2InTaO_7.

© 2009 Elsevier Inc. All rights reserved.

1. Introduction

Since the discovery of photocatalytic splitting of water on TiO_2 electrodes by Fujishima and Honda in 1972 [1], the photocatalytic water splitting using solar energy and semiconductors to generate clean energy hydrogen has attracted increasing attention [2–5]. It is well known that the UV light occupies only about 4% of the whole solar energy while the visible light accounts for 43%. From the viewpoint of a potentially efficient utilization of solar energy, the development of photocatalysts with visible-light response will therefore be valuable for application to H_2 production using solar energy. Oxide materials are plausible candidates of the new photocatalytic material in relation to their higher chemical stability and easier preparation compared with non-oxide materials.

Some tantalates with octahedrally coordinated d^0 configuration, such as $ATaO_3$ (A=Li, Na, K) [6,7], $Sr_2Ta_2O_7$ [8], $RbNdTa_2O_7$ [9], have been well known as promising semiconductor photocatalysts in the last decades. Various indates with octahedrally coordinated d^{10} configuration, such as MIn_2O_4 (M=Ca, Sr, Ba) [10–12] and $Sr_{1-x}M_xIn_2O_4$ (M=Ca, Ba) [13], have also been reported as photocatalysts for water splitting. However, these Ta^{5+}- or In^{3+}-containing compounds are not active under visible light. On the other hand,

the partly filled $4f$ shell plays a key role in photocatalytic reactions and the $4f$ orbital electrons of lanthanides have the effect on reducing the band gap energy of lanthanide complex oxides [9, 14–16]. Especially, some pyrochlore-type $A_2B_2O_7$ (A and B are metal ions) compounds, such as $Ln_2Zr_2O_7$ (Ln=Sm, Nd) [16] and In_2BiTaO_7 [17], have recently been reported as photocatalysts for water splitting under visible light irradiation. Based on above consideration, if appropriate lanthanides ions, Ta^{5+} and In^{3+} are incorporated with an pyrochlore-type crystal structure of semiconductor, a new visible-light-driven photocatalyst with suitable band edges for water splitting might be obtained. It will be interesting to use composite metal oxides involving lanthanide, the p- and d-block metal ions, i.e., metal oxides with $4f$-d^{10}-d^0 configuration, for the development of photocatalysts for water splitting under visible light irradiation since it is thought that hybridization of the sp orbitals of p-block metal ions and the partly filled $4f$ orbital electrons of lanthanides may have a significant effect on the density of states and energy dispersion in the conduction bands and the band gap energy, respectively.

In this paper, we report a new pyrochlore-type ($A_2B_2O_7$) photocatalyst Sm_2InTaO_7 with $4f$-d^{10}-d^0 configuration, in which the B site as core element site is occupied by In^{3+} and Ta^{5+} ions randomly in the charge-balanced manner. Its photocatalytic activity for water splitting was assessed after NiOx-loading under visible light irradiation ($\lambda > 400$ nm). The optimal conditions for high photocatalytic performance were determined experimentally. The photocatalytic activity was compared with that of a pyrochlore-type metal oxide, $Sm_2Zr_2O_7$ [16], with the $4f$-d^0 configuration, and the advantages of the $4f$-d^{10}-d^0 configuration were

---

discussed on the basis of the crystal structure and band structures calculated by the DFT method.

2. Experimental

The polycrystalline samples of the Sm_2InTaO_7 photocatalysts were synthesized by a solid-state reaction method. In_2O_3, Sm_2O_3 and Ta_2O_5 with purity of 99.99% were used as starting materials. Sm_2O_3 was dried before use. The fully mixed chemical powder in a stoichiometric ratio were sintered in air for 52 h in the temperature range 1373–1673 K with intermediate regrinding to complete reaction. The polycrystalline samples of the $Sm_2Zr_2O_7$ photocatalysts were prepared by the reported procedure [16]. To introduce active sites on the surface of the photocatalyst particles, partially oxidized nickel was loaded on the surface of the photocatalyst particles from aqueous $Ni(NO_3)_2$ solution by an impregnation method. The Ni-loaded photocatalyst was first calcined at 350 °C for 1 h in air and reduced in a H_2 atmosphere at 500 °C for 2 h and then treated in an O_2 atmosphere at 200 °C for 1 h. The double-layered structure of metallic Ni and NiO (denoted $NiOx$) was formed on the surface of photocatalyst by a reduction–oxidation procedure [2,18].

The crystal structure of Sm_2InTaO_7 was analyzed by the powder X-ray diffraction (D/Max 2500 VB+, Japan) with $CuK\alpha$ radiation ($\lambda=0.154056$ nm). The data were collected at 295 K with a step scan procedure in the range of $2\theta=5-100°$. The step interval was 0.02° and the scan speed was $1° min^{-1}$. The chemical composition of the compound was determined by field emission scanning electron microscope-X-ray energy dispersion spectrum (SEM-EDS) (Sirion 200, Philips, Netherlands) and inductively coupled plasma atomic emission spectrometers (ICP-AES) (Leeman Prodigy, USA). Surface area and pore volume of the powder sample were measured on a surface area analyzer (Autosorbi/monosorb, Quantachrme, America) by nitrogen absorption at 77 K using the Brunauer–Emmett–Teller (BET) method. Saturated adsorbed amount of O_2 of the powder sample was measured in O_2 ambience by Perkin-Elmer thermogravimetric analysis system. The diffuse reflectance spectra (DRS) of the photocatalyst samples were obtained using a UV–vis scanning spectrophotometer (TU-1901, Beijing-Purkinje, China) at room temperature, and were converted from reflectance to absorbance by the Kubelka–Munk method. The surface chemical states of the photocatalyst samples were measured by X-ray photoelectron spectroscopy (XPS) (ESCALAB MK, England). The microstructures of $NiOx$ on the surface of the photocatalyst samples were measured by transmission electron microscopy (TEM) (TecnaiG20ST, PHILIPS, Netherlands).

The photocatalytic reaction was examined using a closed gas circulation system. The $NiOx$-loaded photocatalyst (1 g) was suspended in distilled water (570 mL) in a quartz inner-irradiation reaction vessel. The reactant solution was evacuated several times to remove air completely prior to irradiation using a 250 W high-pressure Xe arc lamp. For visible irradiation ($\lambda>400$ nm) [5], a circulating sodium nitrite ($NaNO_2$) aqueous solution (2 M) cooled by a flow of cooling water was inserted in the light path used to block ultraviolet (UV) light and remove heat produced by xenon lamp. Moreover, the whole reaction vessel was fooled by a flow of cooling water to make the reactant solution maintained at room temperature during the reaction. The gases evolved in the reaction were analyzed by gas chromatography (Shimadsu GC-8A, Tokyo, Japan; Ar carrier).

The theoretical calculation of the electronic structure of the Sm_2InTaO_7 was carried out based on density function theory with plane-wave pseudopotential method and generalized gradient approximation [19]. The core electrons were replaced by the norm-conserving pseudopotential O $2s^2 2p^4$, In $4d^{10} 5s^2 5p^1$, Ta $4f^{14} 5d^3 6s^3$, and Sm $4f^6 5s^2 5p^6 6s^2$ electrons were treated explicitly.

The kinetic energy cutoff was set to 300 eV, and the unit cell includes $(Sm_2InTaO_7)_2$ structure. The lattice constant and the atomic positions were optimized with finite basis set correction.

3. Results and discussion

Fig. 1 shows the X-ray diffraction patterns of Sm_2InTaO_7 calcined at different temperatures. The power X-ray diffraction analysis showed that Sm_2InTaO_7 calcined at 1573 K and 1673 K was a single phase. In the case of the samples calcined at 1373 K, most of the peaks in X-ray diffraction patterns were attributed to Sm_2InTaO_7, but relatively weak peaks due to In_2O_3 were also observed. With increasing temperature from 1373 to 1673 K, the major peaks became narrower and their intensity increased. The chemical composition of the Sm_2InTaO_7 compound calcined at 1573 K was determined using characteristic X-rays of InL_α, SmL_α, and TaL_α. The composition content was decided using the ZAF (element number, absorption and fluorescence corrections) quantification method. The SEM-EDS analysis showed that the compound had a homogenous atomic distribution with no other additional elements. An average atomic rate of Sm:In:Ta=2.00:0.97(2):1.03(3) was obtained from measurements made at several different points. The exact composition of Sm_2InTaO_7 prepared at 1573 K was also measured by ICP. The ICP-AES chemical composition analysis showed that the chemical formula was determined to be $Sm_{1.99}In_{0.98}Ta_{1.02}O_7$ (normalized to seven oxygens), which was basically in agreement to the nominal starting stoichiometric ratio.

Full-profile structure refinement of the collected powder diffraction data for Sm_2InTaO_7 calcined at 1573 K was performed using the Rietveld program FULLPROF [20]. Positional parameters and isotropic thermal parameters of all atoms of the Sm_2InTaO_7 compound were refined (Table 1). The outcomes of the final refinement indicated that Sm_2InTaO_7 was crystallized in a cubic system with space group $Fd3m$, and the lattice parameter was $a=10.5448(2)$ Å. All of the reflection peaks could be successfully indexed based on the lattice parameter and the space group (see
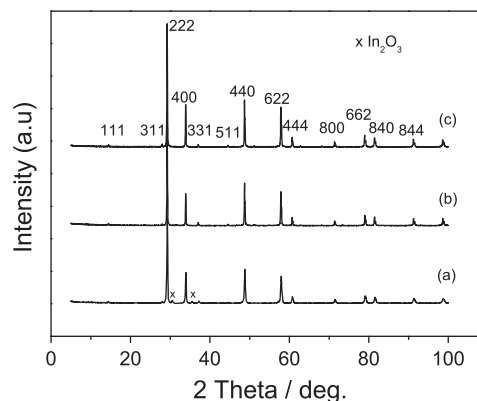

Fig. 1. X-ray diffraction patterns and indexed result of Sm_2InTaO_7 calcined at 1373 K (a), 1573 K (b), and 1673 K (c).

Table 1
Structural parameters of Sm_2InTaO_7 obtained by the Rietveld structure refinement. Sm_2InTaO_7 was prepared by calcination at 1573 K.

Atom	Site	x	y	z	U_{iso} (Å)	Occupancy
Sm	16(d)	0.5000	0.5000	0.5000	0.0123 (5)	1.0
In/Ta	16(c)	0.0000	0.0000	0.0000	0.0028 (8)	0.5
O1	48(f)	0.3302 (3)	0.1250	0.1250	0.010 (4)	1.0
O2	8(b)	0.3750	0.3750	0.3750	0.007 (6)	1.0

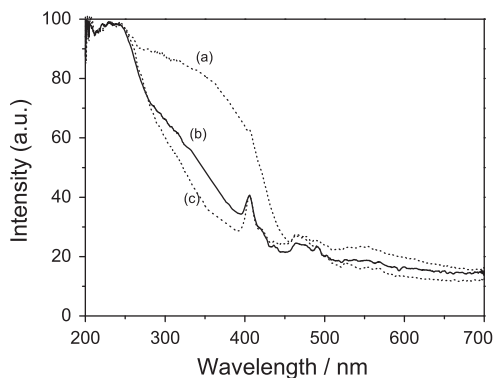**Fig. 2.** UV–vis diffuse reflectance spectrum (DRS) of Sm_2InTaO_7 calculated at 1373 K (a), 1573 K (b), and 1673 K (c).

Fig. 3. Photocatalytic H_2 evolution over 1.0 wt% $NiOx$-loaded Sm_2InTaO_7 under visible-light irradiation. Sm_2InTaO_7 was prepared by calcinations at 1573 K.

Fig. 4. Photocatalytic activity of 1.0 wt% $NiOx$-loaded Sm_2InTaO_7 for H_2 evolution as a function of the calcinations temperature of Sm_2InTaO_7.

Fig. 1). The result of refinements yielded R factors, R_p=7.46%, R_{WP}=10.1% in space group $Fd3m$ when the O atoms are included in the model.

Fig. 2 shows the UV–vis diffuse reflectance spectrum (DRS) of Sm_2InTaO_7 calcined at different temperatures. Sm_2InTaO_7 photocatalyst showed obvious absorption in visible light region ($\lambda > 400$ nm) irrespective of the calcination temperature, which indicated that the prepared Sm_2InTaO_7 had the ability to respond to visible light. An average absorption of < 20% was obtained from 500 to 700 nm and the absorption in wavelength < 420 nm attenuated with increasing calcination temperature and was dramatically reduced upon calcination at 1573 K. This was mainly because it eliminated impurities In_2O_3 and the crystallite size increased with increasing calcination temperature, which resulted in decreasing of light absorption. It should be noted that the onset of the absorption edges of Sm_2InTaO_7 became unclear because several absorptions overlap in visible light range ($\lambda > 400$ nm). This could be attributed to internal transitions in a partly filled Sm $4f$ shell. Actually, the spectra in this region were in accord with those observed in Sm_2O_3 [21]. Two similar results for the overlap with another absorption band had also been reported for the $RbLnTa_2O_7$ (Ln=Pr and Nd) [9] and Bi_2RNbO_7 (R=Y, rare earth) system [22]. The band gaps of the materials were calculated from the absorption spectra by using the equation: $\alpha(hv) = A(hv - Eg)^{n/2}$, where α, v, Eg and A are absorption coefficient, light frequency, band gap, and a constant, respectively. The value of n was determined to be 1 from the absorption spectra, indicating that the optical transitions were all directly allowed for Sm_2InTaO_7. The band gap of Sm_2InTaO_7 prepared at 1573 K was determined to be about 2.81 eV.

Fig. 3 shows photocatalytic H_2 evolution from pure water (570 ml) over 1 wt% $NiOx$-loaded Sm_2InTaO_7 (1.0 g) under visible light irradiation ($\lambda > 400$ nm). The reaction was repeated three times. Clearly, the amount of evolved H_2 gas increased linearly with an increase of irradiation time in three run. The photocatalytic activity slightly decreased in the second run, but no further attenuation occurred in the third run, indicating that $NiOx$-loaded Sm_2InTaO_7 were stable. The XRD patterns of Sm_2InTaO_7 showed no difference before and after the photocatalytic H_2 evolution, also indicating the photocatalyst was stable under the present working condition. The average rate of H_2 evolution in the third run (after about 16 h of reaction time) was about 4.6 μ mol/h for 1 wt% $NiOx$-loaded Sm_2InTaO_7. The turnover number of reacted electrons to the amount of Ni loaded on the surface of Sm_2InTaO_7 reached about 1.5 at 24 h of the reaction time. No H_2 evolution was detected when the light was turned off ('dark test') and the reaction cell was re-evacuated. This result excluded the possibility of H_2 generation from the 'mechano-catalytic mechanism' [23]. All the aforementioned results implied that the H_2 evolution was inherently the result of photocatalytic reaction over the Sm_2InTaO_7 oxide semiconductor.
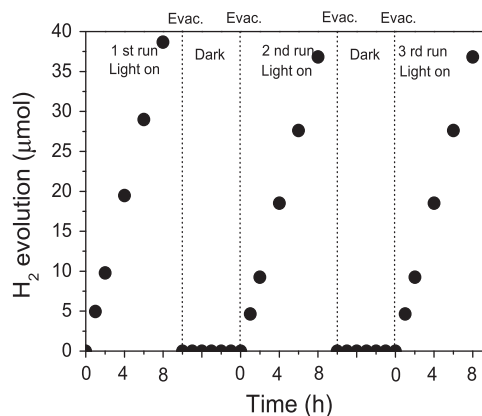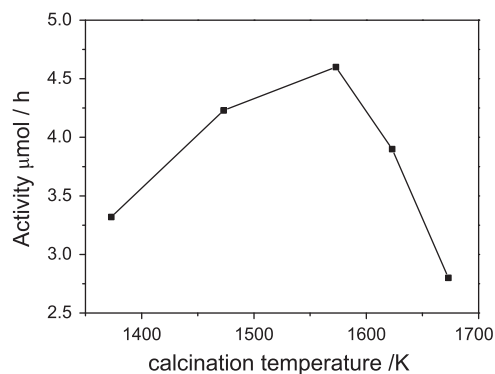
Fig. 4 shows the photocatalytic activity of 1 wt% $NiOx$-loaded Sm_2InTaO_7 for H_2 evolution as a function of the calcination temperature used during Sm_2InTaO_7 preparation. The activity increased with increasing temperature from 1373 K and reached a maximum at 1573 K, beyond which it rapidly decreased. The surface area was 0.67–0.78 m^2/g for calcination below 1573 K and decreased to 0.47 m^2/g for calcination at 1673 K. The reason for the dependence of the photocatalytic activity on the calcination temperature of Sm_2InTaO_7 could be explained as follows: when the calcination temperature was below 1573 K where the activity increased with increasing temperature from 1373 to 1573 K, the XRD images (Fig. 1) showed a considerable increase in the crystallite size of Sm_2InTaO_7 according to a narrowing of the X-ray diffraction peaks. These results demonstrated that the crystallization of Sm_2InTaO_7 was responsible for activity enhancement, since it eliminated impurities and structural imperfections that frequently acted as traps for charge recombination. When the calcination temperature was above 1573 K, 1 wt% $NiOx$ on the Sm_2InTaO_7 surface was excess due to the reduction of the surface area of Sm_2InTaO_7 and the relationship between the amount of $NiOx$ loaded and photocatalytic activity (see Fig. 5) indicated that the excess $NiOx$ on the Sm_2InTaO_7 surface lowered the activity. The agglomeration of $NiOx$ particles readily occurred (see Fig. 6) when large amounts of $NiOx$ were loaded for a small surface area of Sm_2InTaO_7, producing large $NiOx$ particles, which resulted in decrease of the density of photocatalytic active sites. Fig. 7 shows a TEM image of the 1 wt% $NiOx/Sm_2InTaO_7$ photocatalyst prepared by calcination at 1573 K. Nearly spherical $NiOx$ particles were distributed on the surface of Sm_2InTaO_7 and the
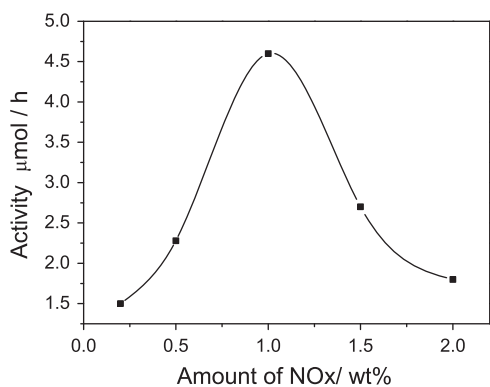
Fig. 5. Photocatalytic activity of NiOx-loaded Sm$_2$InTaO$_7$ for H$_2$ evolution as a function of the amount of NiOx loading. Sm$_2$InTaO$_7$ was prepared by calcinations at 1573 K.

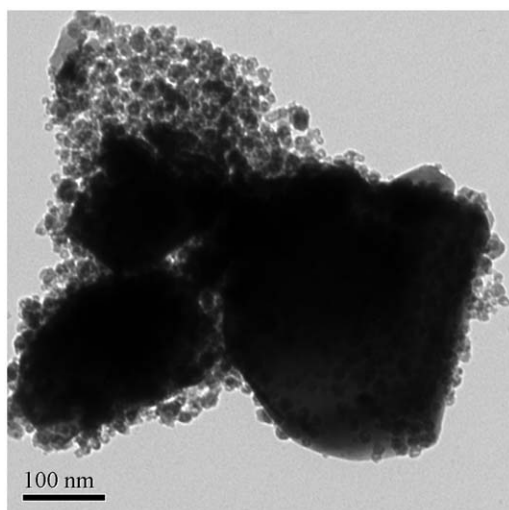Fig. 7. TEM image of the 1 wt% NiOx/Sm$_2$InTaO$_7$ photocatalyst prepared by calcinations at 1573 K.

Fig. 6. TEM micrograph of 1.0 wt% NiOx/Sm$_2$InTaO$_7$ photocatalyst prepared by calcinations at 1673 K.

Fig. 8. Ni 2p XPS spectra of 1 wt% NiOx/Sm$_2$InTaO$_7$: (a) before photocatalytic water splitting, and (b) after photocatalytic water splitting. Asterisks denote positions of the satellite peaks.

sizes of NiOx particles were about 16 nm. These results indicated that a high dispersion of small NiOx particles was essential for high photocatalytic performance of NiOx-loaded Sm$_2$InTaO$_7$.

The XPS spectra of 1 wt% NiOx/Sm$_2$InTaO$_7$ before and after photocatalytic water splitting shown in Fig. 8 reveal the chemical status of nickel on the surface of Sm$_2$InTaO$_7$. It is known that the binding energies of the Ni 2$P_{3/2}$ level for metallic nickel and NiO were 852.9 and 855.8 eV, respectively [24]. The binding energy peaks of the Ni 2$P_{3/2}$ level for NiOx/Sm$_2$InTaO$_7$ before photocatalytic water splitting was 854.6 eV (shown in Fig. 8 (a)). The binding energy value was attributed to a combination of NiO and Ni, indicating that the formation of partially oxidized nickel as an enhancer of catalytic activity. The Ni 2$P_{3/2}$ level for NiOx/Sm$_2$InTaO$_7$ after photocatalytic water splitting exhibits a slight positive shift to 856.1 eV (shown in Fig. 8(b)), indicating that Ni(OH)$_2$ was formed after photocatalysis in aqueous solution [25].

However, no sign of O$_2$ evolution was observed in these experiments with NiOx-loaded Sm$_2$InTaO$_7$ photocatalysts. The same phenomenon has arisen over TiO$_2$ [26], Bi$_2$InNbO$_7$ [27], MCo$_{1/3}$Nb$_{2/3}$O$_3$ (M=Ca, Sr, and Ba) [28], and so on. On the one hand, it was proposed that there were both physisorbed and chemisorbed O$_2$ molecules on the surface of TiO$_2$ through low-energy photon irradiation, where the physisorbed O$_2$ was produced through the neutralization of chemisorbed O$_2^-$ species by photogenerated holes
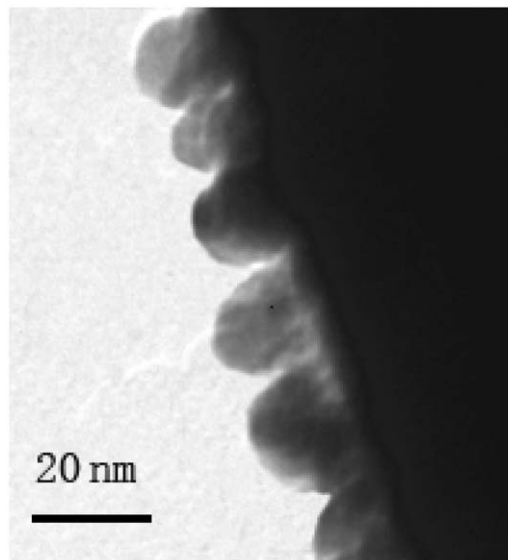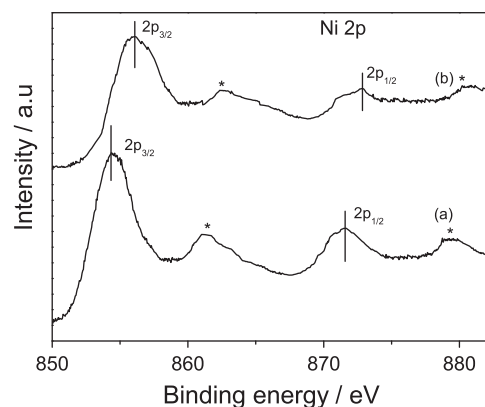
[26]. On the other hand, saturated adsorbed amount of O$_2$ had been measured by an indirect method (thermogravimetric analysis). Saturated adsorbed amount of O$_2$ for 1 wt% NiOx-loaded Sm$_2$InTaO$_7$ at 305 K was about 100 μmol/g. Oxygen evolution should be very small in this experiment. Therefore, it was completely possible to notice no oxygen evolution was observed from pure water in this experiment. In addition, a series of the diffusions of these physisorbed and chemisorbed oxygen molecules along or over the crystalline boundaries also may be responsible for the 'absent' oxygen [29]. Further study of the photoadsorption of oxygen on these samples under visible light irradiation is in progress, which is believed to supply more concrete information.

As a comparison, the reaction of H$_2$ evolution over NiOx-loaded Sm$_2$Zr$_2$O$_7$ photocatalyst was carried out under the same condition. As shown in Fig. 9, the activity of NiOx-loaded Sm$_2$Zr$_2$O$_7$ was low. The rates of H$_2$ evolution over NiOx-loaded Sm$_2$Zr$_2$O$_7$ was 0.33 μmol/h. The surface area of Sm$_2$Zr$_2$O$_7$ prepared by a solution reaction method was 6.36 m^2/g while the surface area of Sm$_2$InTaO$_7$ prepared by the solid-state method was only 0.67 m^2/g, indicating that the surface area was not the most important factor in deciding the different activities of the both photocatalysts.

It is generally believed that the crystal structure of photo-catalyst play a crucial role in the photocatalytic activities. The schematic structural diagram of Sm_2InTaO_7 with pyrochlore-type
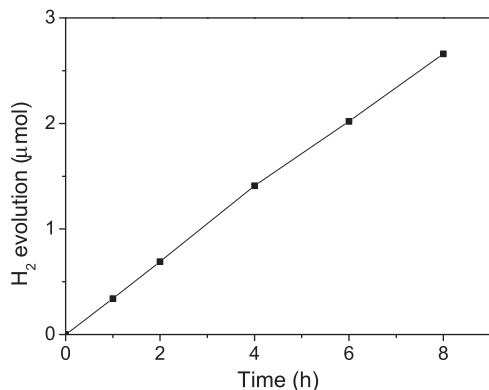

Fig. 9. Photocatalytic H_2 evolution over 1.0 wt% NiOx-loaded $Sm_2Zr_2O_7$ under visible-light irradiation. $Sm_2Zr_2O_7$ was prepared by a solution reaction method.
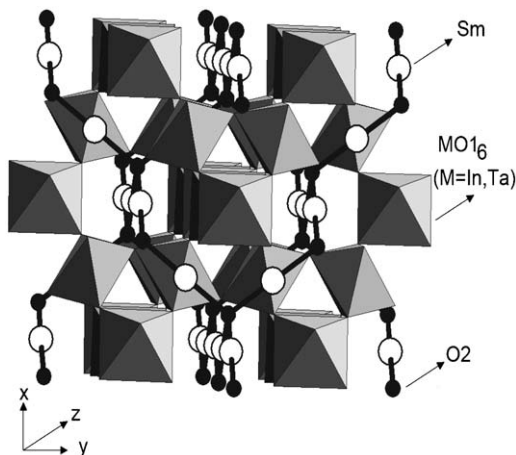

Fig. 10. Schematic structural diagram of Sm_2InTaO_7. Sm_2InTaO_7 consist of a three-dimensional network structure of corner-linked $MO1_6$ (M=In and Ta) octahedral, connecting each other into $[MO1_3]_a$ chains along [001].

structure is depicted in Fig. 10. It shows that the whole structure, similar to that of the Bi_2InNbO_7 compound [30], consists of the three-dimensional network of corner-linked $MO1_6$ (M=In and Ta) octahedra. The $MO1_6$ octahedra connect each other into $[MO1_3]_a$ chains along [001] and the Sm ions are located in between $MO1_6$ octahedral. Both the InO_6 and TaO_6 octahedrons in Sm_2InTaO_7 are heavily distorted. The distortion of BO_6 polyhedra in $A_2B_2O_7$-type pyrochlore structures results in their lattice distortion which is one of the important parameter for charge separation and contributes to enhance the photocatalytic activity [8,31]. A correlation between photocatalytic activity and lattice distortion has been demonstrated in a series of pyrochlore-type structure metal oxide photocatalysts [32]. Information on the lattice distortion can be obtained from the O ($48f$) parameter x in the pyrochlore-type $A_2B_2O_7$ structure. The lattice distortion is equal to 0.375—the O ($48f$) parameter x [32]. For $Sm_2Zr_2O_7$, x=0.3359 [16], the lattice distortion was evaluated to be 0.0391 while the lattice distortion was evaluated to be 0.0448 for the Sm_2InTaO_7 photocatalyst. Thus, the present results for the NiOx-loaded Sm_2InTaO_7 showing high photocatalytic performance were in line with the correlation between activity and lattice distortion. Due to the presence of two metal ions with different sizes in the same site in the unit cell, the ease of formation of distorted octahedral units was the advantage of $4f$-d^{10}-d^0 composite metal oxides over metal oxides with the $4f$-d^0 configuration.

It is also generally believed that the band structure of photo-catalyst play a decisive role in the photocatalytic activities. Prokofiev et al. [33] had studied periodicity in the optical band gap variation of rare earth sesquioxides. According to their results, the occupied $4f$ band in rare earth sesquioxides lay above the O $2p$ level, and thus the $4f$–d transition determined the band gaps. The same considera-tion may be made for the Sm_2InTaO_7 compound. In addition, $5s$ and $5p$ orbitals of In^{3+} with octahedrally coordinated d^{10} configuration also may contribute to the conduction band of Sm_2InTaO_7. To confirm above consideration, the theoretical calculation of the electronic structure of the Sm_2InTaO_7 was carried out based on density function theory with plane-wave pseudopotential method and generalized gradient approximation. Structural parameters of Sm_2InTaO_7 obtained by the Rietveld structure refinement were used in DFT calculation. As the Sm $4f$ orbitals had smaller overlap and lower ionization potential, the self-consistent field (SCF)
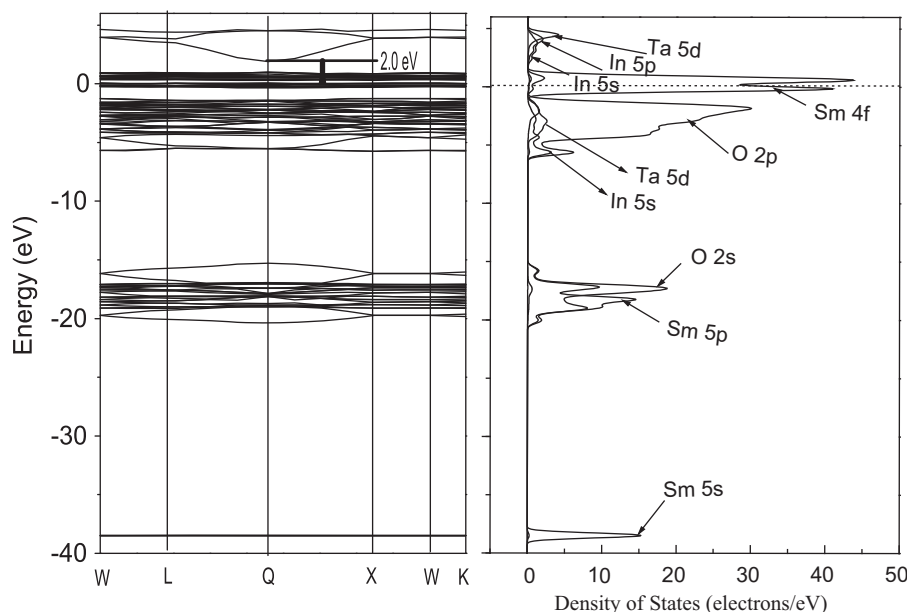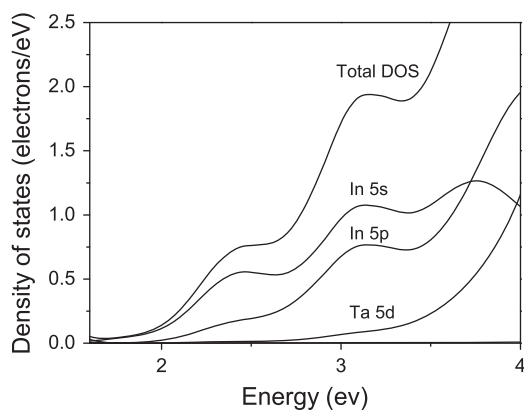

Fig. 11. Band description and DOS for Sm_2InTaO_7.

Fig. 12. Total and partial DOS of Sm_2InTaO_7 around the bottom of the conduction band.

convergence was not good. Therefore, a fractional occupation technique was employed, which allows for the withdrawal and accumulation of a small amount of electron density in the top of the valence band and bottom of the conduction band [34]. Fig. 11 shows the band structure and density of state (DOS) of Sm_2InTaO_7. The top of the valence band (the Fermi level) is set to be zero on the ordinate. Very strong and narrow double peaks in DOS represented the localized character of Sm 4f levels. The Sm 4f bands existed above the top of the O 2p band and the valence band edge of Sm_2InTaO_7 became higher to decrease Eg. The occupied bands were the Sm 5s, O 2s+Sm 5p, O 2p+In 5s+Ta 5d, and Sm 4f bands in increasing order of energy, where the last was the valence band. The bottom of the unoccupied level (conduction band) was composed of the In 5s+In 5p, and Ta 5d atomic orbitals in the order of increasing energy. Both the valence band maximum and the conduction band minimum were located at the Q point, indicating that Sm_2InTaO_7 was a direct band gap semiconductor. The valance band was rather flat, and its dispersion was small. By contrast, the conduction band had a strong dispersion. The DFT calculation indicated the band gap of Sm_2InTaO_7 was 2.0 eV. The value was smaller than that obtained experimentally, which should be pointed out as a common feature of DFT calculations. This underestimation was an artifact of the GGA method used for this calculation [35]. To obtain more clear and exact information on the conduction band of Sm_2InTaO_7, partial DOS of Sm_2InTaO_7 around the bottom of the conduction band was shown in Fig. 12. The bottom of the CB in Sm_2InTaO_7 were composed of the hybridized In 5s and 5p orbitals, which revealed that Sm_2InTaO_7 had partial characteristic electronic structure of a d^{10} semiconductor. This result was obviously different from the Zr 4d orbital contributing mainly at the bottom of the CB in $Sm_2Zr_2O_7$ [16]. The hybridized In 5s and 5p orbitals (see Fig. 11) led to a strong dispersion. In the electron transfer from the Sm 4f orbital to the hybridized In 5s5p orbitals upon illumination, the strong dispersion in the conduction bands generated photoexcited electrons with high mobility, which was evidently associated with the high photocatalytic performance of NiOx-loaded Sm_2InTaO_7. Thus, from a viewpoint of band structures, the contribution of In 5s5p to the conduction bands was responsible for the high photocatalytic activity of NiOx-loaded Sm_2InTaO_7. The contribution of the sp orbitals of p-block metal ions to the conduction bands was also the advantage of $4f$-d^{10}-d^0 composite metal oxides over metal oxides with the $4f$-d^0 configuration.

4. Conclusions

The pyrochlore-type compound Sm_2InTaO_7 with $4f$-d^{10}-d^0 configuration was synthesized by a solid-state reaction method.

The Sm_2InTaO_7 was found to be a new stable visible-light-response photocatalyst for H_2 evolution from pure water after NiOx-loading and the combination of well-crystallized Sm_2InTaO_7 with highly dispersed NiOx particles resulted in high photocatalytic performance. The $4f$-d^{10}-d^0 configuration was useful for photocatalysis from the viewpoint of both crystal and electronic structures.

Acknowledgments

Appendix A. Supplementary material

Supplementary data associated with this article can be found in the online version at doi:10.1016/j.jssc.2009.10.023.

References

[1] A. Fujishima, K. Honda, Nature 238 (1972) 37.
[2] Z. Zou, J. Ye, K. Sayama, H. Arakawa, Nature 414 (2001) 625.
[3] R. Asahi, T. Morikawa, T. Ohwaki, K. Aoki, Y. Taga, Science 293 (2001) 269.
[4] H. Kato, K. Asakura, A. Kudo, J. Am. Chem. Soc. 125 (2003) 3082.
[5] D. Lu, T. Takata, N. Saito, Y. Inoue, K. Domen, Nature 440 (2006) 295.
[6] T. Ishihara, H. Nishiguch, K. Fukamachi, Y. Takita, J. Phys. Chem. B 103 (1999) 1.
[7] H. Kato, A. Kudo, J. Phys. Chem. B 105 (2001) 4285.
[8] A. Kudo, H. Kato, S. Nakagawa, J. Phys. Chem. B 104 (2000) 571.
[9] M. Machida, J. Yabunaka, T. Kijima, Chem. Mater. 12 (2000) 812.
[10] J. Sato, S. Saito, H. Nishiyama, Y. Inoue, J. Phys. Chem. 105 (2001) 6061.
[11] J. Sato, S. Saito, H. Nishiyama, Y. Inoue, Chem. Lett. (2001) 868.
[12] J. Yin, Z. Zou, J. Ye, J. Mater. Res. 17 (2002) 2201.
[13] J. Sato, S. Saito, H. Nishiyama, Y. Inoue, J. Phys. Chem. 107 (2003) 7975.
[14] M. Machida, J. Yabunaka, T. Kijima, J. Phys. Chem. B 105 (2001) 3289.
[15] M. Uno, A. Kosuga, M. Okui, K. Horisaka, S. Yamanaka, J. Alloys Compd. 400 (2005) 270.
[16] M. Uno, A. Kosuga, M. Okui, K. Horisaka, H. Muta, K. Kurosaki, S. Yamanaka, J. Alloys Compd. 420 (2006) 291.
[17] J.F. Luan, Z.G. Zou, M.H. Lu, G.Y. Luan, Y.F. Chen, Res. Chem. Intermediat. 32 (2006) 31.
[18] A. Kudo, K. Sayama, A. Tanaka, K. Asakura, K. Domen, K. Maruya, T. Onishi, J. Catal. 120 (1989) 337.
[19] M.D. Segall, L.D. Lindan, M.J. Probert, C.J. Pickard, P.J. Hasnip, S.J. Clark, M.C. Payne, J. Phys. Condens. Matter 14 (2002) 2717.
[20] J. Rodriguez-Carvajal, Fullprof 2k, Version 3.4 (November 2005), Laboratoire Leon, Brillouin (CEA/CNRS), CEA-Saclay, 91191 Gifsur-Yvette Cedex, France.
[21] J.K. Ryan, Chr.K. Jorgensen, J. Phys. Chem. 7 (1966) 2845.
[22] Z. Zou, J. Ye, H. Arakawa, J. Phys. Chem. B 106 (2002) 517.
[23] K. Domen, J.N. Kondo, M. Hara, T. Takata, Bull. Chem. Soc. Jpn. 73 (2000) 1307.
[24] J.F. Moulder, J. Chastain, R.C. King, Handbook of X-ray Photoelectron Spectroscopy: A Reference Book of Standard Spectra for Identification and Interpretation of XPS Data, Physical Electronics, Eden Prairie, Minnesota, 1995.
[25] K. Domen, A. Kudo, T. Onishi, N. Kosugi, H. Kuroda, J. Phys. Chem. 90 (1986) 292.
[26] A.L. Linsebigler, G. Lu, J.T. Yates Jr., Chem. Rev. 95 (1995) 735.
[27] Z. Zou, J. Ye, R. Abe, H. Arakawa, Catal. Lett. 68 (2000) 235.
[28] J. Yin, Z. Zou, J. Ye, J. Phys. Chem. B 107 (2003) 4936.
[29] A.M. Svensson, S. Sunde, K. Nisancioglu, J. Electrochem. Soc. 145 (1998) 1390.
[30] Z. Zou, J. Ye, H. Arakawa, J. Mater. Sci. Lett. 19 (2000) 1987.
[31] Y. Inoue, M. Kohno, S. Ogura, K. Sato, Chem. Phys. Lett. 267 (1997) 72.
[32] J. Wang, Z. Zou, J. Ye, J. Phys. Chem. Solids 66 (2005) 349.
[33] A.V. Prokofiev, A.L. Shelykh, A.V. Golubkov, I.A. Smirnov, J. Alloys Compd. 219 (1995) 72.
[34] A. Ishikawa, T. Takata, J.N. Kondo, M. Hara, H. Kobayashi, K. Domen, J. Am. Chem. Soc. 124 (2002) 13547.
[35] J. Sato, N. Saito, Y. Yamada, K. Maeda, T. Takata, J.N. Kondo, M. Hara, H. Kobayashi, Y. Inoue, K. Domen, J. Am. Chem. Soc. 127 (2005) 4150.